

Efficient completeness inspection using real-time 3D color reconstruction with a dual-laser triangulation system

Matteo Munaro and Edmond Wai Yan So and Stefano Tonello and Emanuele Menegatti

Abstract In this chapter, we present the final system resulting from the European Project "3DComplete" aimed at creating a low-cost and flexible quality inspection system capable of capturing 2.5D color data for completeness inspection. The system uses a single color camera to capture at the same time 3D data with laser triangulation and color texture with a special projector of a narrow line of white light, which are then combined into a color 2.5D model in real-time. Many examples of completeness inspection tasks are reported which are extremely difficult to analyze with state-of-the-art 2D-based methods. Our system has been integrated into a real production environment, showing that completeness inspection incorporating 3D technology can be readily achieved in a short time at low costs.

1 Introduction

An important application of machine vision is quality control, and in particular completeness inspection - checking the presence or absence of parts, identifying their type, and determining their position and orientation. Until recently, many systems have relied on 2D-based image analysis [4]. However, without depth information, 2D machine vision systems have various shortcomings that limit their capabilities and robustness. For example, they cannot reliably detect parts in front of a background of similar color or reflectance (i.e., low contrast). Also, difficulties often arise when dealing with non-rigid objects, such as hoses and cables, that may

Matteo Munaro, Edmond Wai Yan So and Emanuele Menegatti
Intelligent Autonomous Systems Laboratory, University of Padova, via Gradenigo 6a,
35131 Padova, Italy, e-mail: munaro@dei.unipd.it, edmond.waiyan.so@gmail.com, emg@dei.unipd.it

Stefano Tonello
IT+Robotics Srl, Strada Prima 11, 35129 Padova, Italy, e-mail: stefano.tonello@it-robotics.it

change their position and lead to occlusions so that the parts to be inspected are not fully visible. As commercial 3D scanners become more affordable, the manufacturing industry is increasingly looking to incorporate 3D scanning technology to overcome the limitations of 2D machine vision [1]. The 3DComplete European project (<http://3dcomplete.eu>) is carried out by a consortium of small business enterprises and research institutes in Europe aiming to develop 3D completeness inspection systems that are similar to existing 2D inspection systems in terms of speed, ease of use and integration, but provide improved functionality by incorporating 3D data. While commercial 3D sensing products already exist, they are designed mainly for reverse-engineering and precise metrology, and have prohibitively high costs. A major aim of the project is to create low-cost 3D sensing solutions that are suitable for completeness inspection.

This chapter describes one of the technologies being developed under this project, called *extended 2.5D inspection*, where 3D information obtained by laser triangulation is combined with color and texture information obtained with a camera. To demonstrate this technology, the University of Padova and IT+Robotics, two of the participants in the project, have developed a prototype color scanner using commercial-off-the-shelf components to showcase a low-cost sensor suite that can be readily deployed in an industrial assembly line setting to perform 3D completeness inspection.

A typical problem of laser triangulation systems is the trade-off between depth resolution and sensing range. Many commercial solutions, like the SICK Ruler, have a fixed baseline. These products are already precisely calibrated, but have the drawback that they work only at a fixed resolution and sensing range. Moreover, the problem of occlusions cannot be mitigated by adding more laser projectors in different positions. Other solutions such as the SICK Ranger offer higher configurability by allowing range to be acquired from more than one laser, but the calibration between range and texture data in order to register the two types of information is left to the end user.

Our system, on top of being cost-effective, provides the possibility to use two lasers for range acquisition and register the depth acquisition with the colored texture acquired in the same pass. Moreover, it offers full flexibility in the lasers position, thus allowing also asymmetric configurations that capture both the macroscopic geometry of the scanned object as well as minute surface details that may be important for defect inspection.

The reconstruction and inspection software has been developed using open-source libraries with permissive licenses. This demonstrates that in addition to inexpensive hardware, the software development cost for 2.5D technology can also be very low.

The remainder of the chapter is organized as follows: in Section 2, the main concepts related to laser triangulation systems are explained, while our Dual-Laser Triangulation System is presented in Section 3. Section 4 details the calibration procedure we developed for our system and Section 5 describes the reconstruction pipeline and products. In Section 6, we report some examples of completeness in-

spection we can perform with the output of our system and an industrial solution is also presented in Section 7. Finally, conclusions are drawn in Section 8.

2 Laser triangulation

The 2.5D color scanner being developed uses laser triangulation as the underlying technology to obtain 3D information. A laser triangulation system, also known variously as a laser striper and a laser stripe profiler, is a form of structured light system.

As shown in Fig. 1, such a system comprises of an illuminating laser source and a camera. Using the triangulation principle, with known baseline b and triangulation angle α between the laser and camera, the distance Z to the scanned object can be determined. The system parameters b and α affects several aspects of performance, such as the sensing range, depth resolution, occlusion, and laser reflectance, which we briefly describe in the following using 2D geometry. A more thorough analysis can be found in [6].

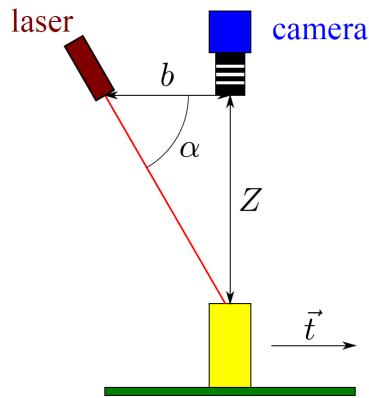


Fig. 1 General Configuration of a Laser Triangulation System.

2.1 Sensing range

As shown in Fig. 2, for a laser located at \mathcal{O}_L , and a camera located at \mathcal{O}_C with a field-of-view of ϕ , with baseline b between the laser and camera, and triangulation angle α between their principal axes, the minimum distance Z_{min} and maximum distance Z_{max} that can be measured by the system are:

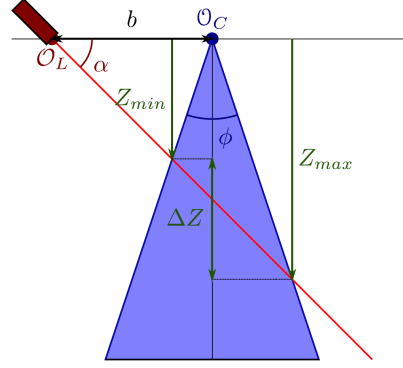


Fig. 2 Sensing Range of a Laser Triangulation System.

$$Z_{min} = \frac{b \sin \alpha \cos \frac{\phi}{2}}{\cos \left(\alpha - \frac{\phi}{2} \right)} = \frac{b}{\frac{1}{\tan \alpha} + \tan \left(\frac{\phi}{2} \right)} \quad (1)$$

$$Z_{max} = \frac{b \sin \alpha \cos \frac{\phi}{2}}{\cos \left(\alpha + \frac{\phi}{2} \right)} = \frac{b}{\frac{1}{\tan \alpha} - \tan \left(\frac{\phi}{2} \right)} \quad (2)$$

The total sensing range $\Delta Z = Z_{max} - Z_{min}$ is thus:

$$\Delta Z = b \sin \alpha \cos \frac{\phi}{2} \left(\frac{1}{\cos \left(\alpha + \frac{\phi}{2} \right)} - \frac{1}{\cos \left(\alpha - \frac{\phi}{2} \right)} \right) = \frac{2b \tan \left(\frac{\phi}{2} \right)}{\frac{1}{\tan^2 \alpha} - \tan^2 \left(\frac{\phi}{2} \right)} \quad (3)$$

Thus, Z_{min} , Z_{max} , and ΔZ all increase with increasing baseline b and triangulation angle α .

2.2 Depth resolution

Using the pinhole camera model, for a camera with focal length f and pixel size $s_{z_{px}}$, the angular resolution is $\theta = \tan^{-1} \frac{s_{z_{px}}}{f}$. As shown in Fig. 3, with baseline b and triangulation angle α between the laser and camera, the depth resolution res at distance Z along the optical axis is:

$$res = Z \left(\frac{\cos \alpha \cos \theta}{\cos (\alpha - \theta)} - 1 \right) = Z \frac{1}{\frac{1}{\tan \alpha \tan \theta} - 1} \quad (4)$$

Thus, the depth resolution res deteriorates with increasing triangulation angle α and at increasing depth Z .

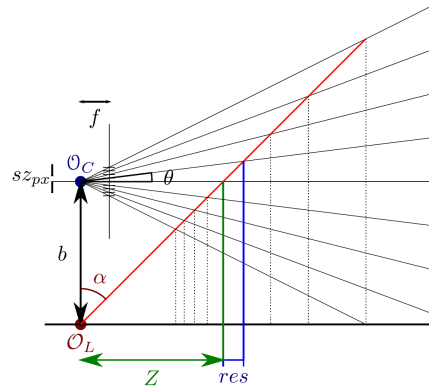


Fig. 3 Depth Resolution in a Laser Triangulation System.

2.3 Occlusion

As shown in Fig. 4, in a laser triangulation system, occlusion can occur either when the laser light is blocked by an object from reaching another surface, or when the camera is blocked by an object from imaging the laser light on another surface. We will refer to them respectively as projection path occlusion and imaging path occlusion.

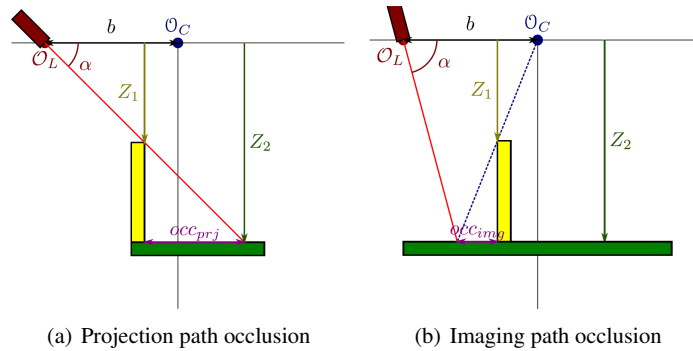


Fig. 4 Occlusion in a Laser Triangulation System.

We can quantify occlusion by measuring the distance on a horizontal surface lying at distance Z_2 that would be occluded by an object at distance Z_1 . For a given baseline b and triangulation angle α , the amount of projection path occlusion and imaging path occlusion are respectively:

$$occ_{prj} = \frac{Z_2 - Z_1}{\tan \alpha} \tag{5}$$

$$occ_{img} = \left(1 - \frac{Z_2}{Z_1}\right) \left(b - \frac{Z_2}{\tan \alpha}\right) \quad (6)$$

Thus, with increasing triangulation angle α , projection path occlusion occ_{prj} decreases while imaging path occlusion occ_{img} increases.

2.4 Laser reflectance

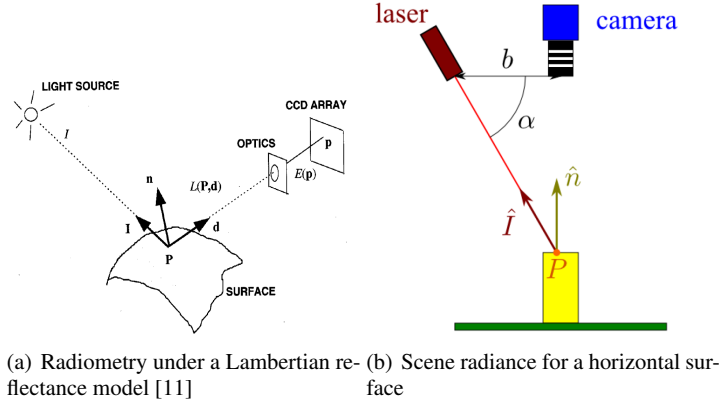


Fig. 5 Laser Reflectance in a Laser Triangulation System.

The amount of light reflected at point P on a surface is known as the scene radiance L . Using the Lambertian reflectance model, as shown in Fig. 5a, under illumination by a source at direction $\hat{I} = I / \|I\|$ and intensity $\|I\|$, the scene radiance $L(P)$ of a point P on a diffuse or matte surface with surface normal \hat{n} and surface albedo ρ is [11]:

$$L = \rho I^T \hat{n} = \rho \|I\| \hat{I}^T \hat{n} \quad (7)$$

As shown in Fig. 5b, for a horizontal surface, $\hat{I}^T \hat{n} = \sin \alpha$, and $L_{horizontal}(P) = \rho \|I\| \sin \alpha$. Thus, scene radiance increases with increasing triangulation angle α .

The actual amount of light imaged by a camera, known as the image irradiance E , and measured as the power of light received per unit area at a point p on the image plane, is [11]:

$$E(p) = L(P) \frac{\pi}{4} \left(\frac{D}{f}\right)^2 \cos^4 \Theta \quad (8)$$

Here, Θ is the angle between the camera's optical axis and the ray from p to P , and D is the diameter of the lens. Thus, for a given scene radiance L , the image irradiance E decreases for pixels lying further from the principal image point $[u_c, v_c]$.

3 Dual-laser triangulation system

The 2.5D color scanner that was developed uses laser triangulation as the underlying technology to obtain 3D information. This is augmented with color texture information from a color CCD camera. As we will describe in Section 5, the depth, texture, and color information can be used either individually or in combination to produce a variety of data representations. This leads to a high degree of flexibility and robustness in creating inspection algorithms according to the task to be performed. Fig. 6 shows the layout of the color 2.5D scanner that was developed, which we call a *Dual-Laser Triangulation System* (DLTS). It consists of a color CCD camera, two line lasers, and a pair of line lights mounted over a translational platform. The major features of this configuration are described below.

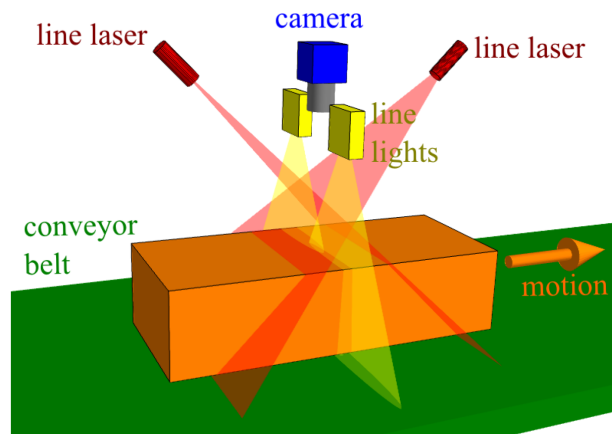


Fig. 6 Dual-Laser Triangulation System.

3.1 *Dual-laser for reducing occlusions*

In designing our system for completeness inspection, the main focus was on being able to reconstruct large overall features of a scanned object. As a result, an important factor was to minimize the amount of occlusions in order to detect all the components on an object reliably. Thus, two line lasers are used in our configura-

tion. Although a system with two cameras and one line laser ([10], [12]) can also be used to reduce occlusions, a dual-laser configuration is more cost effective, as an additional camera is usually more expensive than an additional line laser.

Fig. 7a shows an example product to be inspected. Fig. 7b shows a point cloud reconstruction of this object obtained with a single-pass scanning, with the points reconstructed by the two lasers differentiated by color. In particular, opposing vertical faces are often only detectable by one of the two lasers, as shown in Fig. 7b. A white connector highlighted in red in the images is of particular interest for inspection. It is located close to the base and surrounded by many other components; while it would be occluded to one of the lasers, a dual laser configuration allows the component to be reliably detected regardless of the scanning direction.

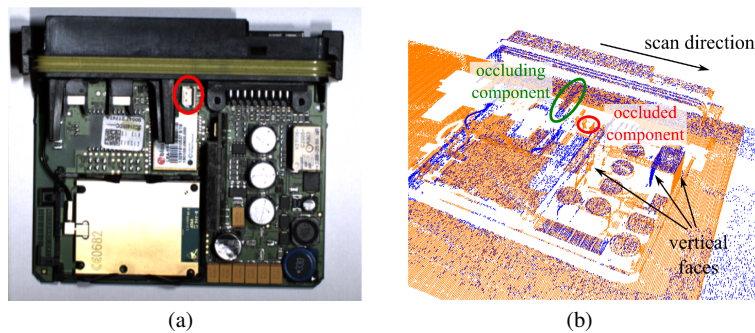


Fig. 7 Reduction of occlusions with dual lasers. (a) Color texture of example product, with white connector to be inspected highlighted in red. (b) Point cloud obtained with a single-pass scanning, with points reconstructed by the two lasers differentiated by color; the white connector is occluded to one of the lasers but visible to the other.

3.2 Line light for simultaneous color texture acquisition

Two line lights positioned on either side of the camera and aligned in the same direction of the laser lines (Fig. 8) are used to illuminate precisely the central part of the imaged scene, so that color texture information of the scanned object can be acquired simultaneously with the images of the laser lines, as shown in Fig. 9.

The line light consists of a series of low-power LEDs, and the illumination is focused by a cylindrical lens to produce the required beam width. For our operations, the beam is focused to a width of 10mm at an operating distance of $\sim 300\text{mm}$. This can be easily modified by changing the relative distance between the LEDs and the lens for small adjustments, and lens diameter for larger adjustments. The small dimensions of the line lights enable them to be easily integrated with the sensor assembly, and can be produced very economically. This solution was designed and produced for us by LightCube srl (<http://www.light-cube.com>).

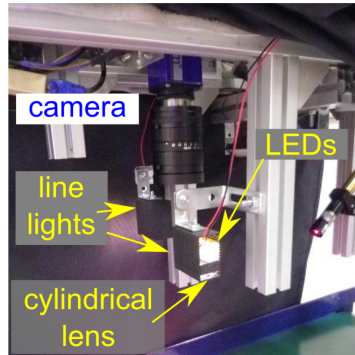


Fig. 8 Line light assembly.

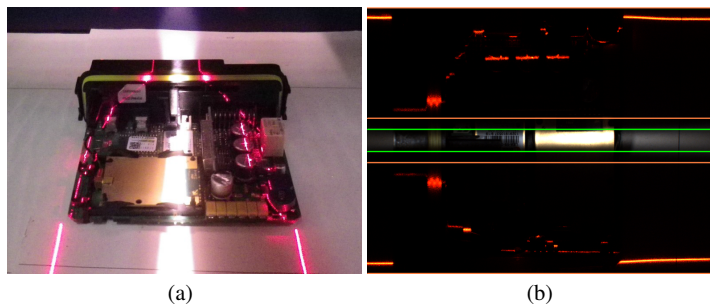


Fig. 9 Simultaneous laser lines and color texture acquisition. (a) Illumination of object by line lights and line lasers. (b) The imaged scene is separated into three regions for simultaneous laser lines and texture acquisition.

By acquiring laser lines and texture together in the same image, the number of image rows available for laser line detection is decreased, leading to a reduction in the depth resolution that would otherwise be achievable. However, when using a dual-laser configuration, a small separation should be reserved between the image regions of the two lasers in order to avoid the laser lines crossing into the other region. Furthermore, only very small number of image rows (5-10 in our operations) is required for obtaining a continuous texture image. Thus, in our implementation, there is practically no impact on the maximum achievable depth resolution.

An alternative approach for acquiring texture information would be to operate the lasers and an area lighting system in an alternating sequence, so laser line and color images are acquired separately in succession. However, this would require additional hardware for synchronization, and the frame rate of the camera would have to be divided between the two types of images, reducing reconstruction density.

3.3 High configurability

Another advantage of using a dual-laser configuration is that the lasers can be positioned asymmetrically to achieve different sensing range and depth resolutions (Fig. 10). In general, the trade-off with using a smaller triangulation angle α to achieve a higher depth resolution res is a reduction in the sensing range ΔZ , as well as an increase in occlusions (Fig. 10a). However, in a dual-laser configuration, the two lasers can effectively complement each other in terms of these opposing factors. Thus, one laser can be used to capture the macroscopic geometry of the scanned object, while the other laser can be used to focus on minute surface details (Fig. 10b).

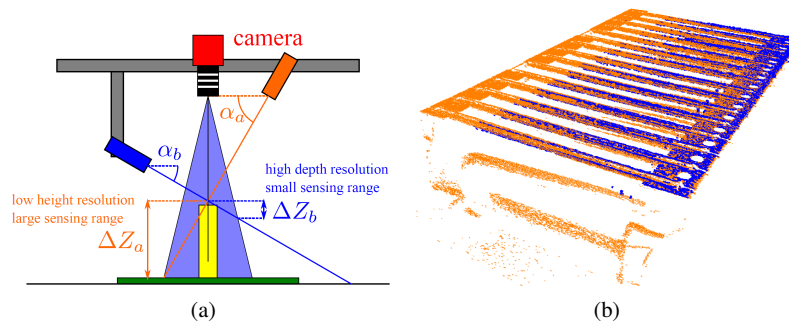


Fig. 10 Asymmetric dual lasers configuration. (a) Two lasers can be configured for different depth resolution and sensing range. (b) This allows one laser to be used for obtaining the macroscopic geometry, while the other is used to obtain minute surface details.

3.4 Hardware components and system prototype

Our DLTS sensor suite is assembled using readily available commercial machine vision components. The chosen color CCD camera has a resolution of 1600x1200, with a full-frame frame rate of 28.1 *fps*. It is paired with a 16mm lens. The 5mW red lasers emit at a wavelength of 635nm, and its accompanying focusable optics are used to create a Gaussian line profile.

To test the performance of the DLTS in a realistic assembly line environment, a system prototype was built by mounting the DLTS sensor suite over a conveyor belt (Fig. 11). The system is enclosed using dark curtains to prevent ambient lighting from interfering with image acquisition. However, in an industrial setting, the need for curtains can be avoided by using more powerful lasers.

The lasers, line lights, and conveyor belt are controlled by a PC workstation through a National Instruments USB-6009 digital I/O unit; this function would nor-

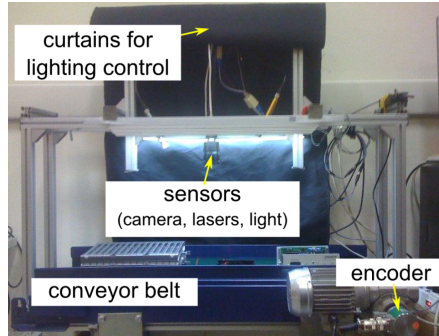


Fig. 11 System prototype with DLTS mounted over conveyor belt.

mally be replaced by a PLC in an industrial environment. The encoder signals are directly connected into the camera, so that the conveyor belt position is precisely recorded with each frame at the time of acquisition. The camera transmits image and encoder data to the workstation through a Gigabit Ethernet link (Fig. 12).

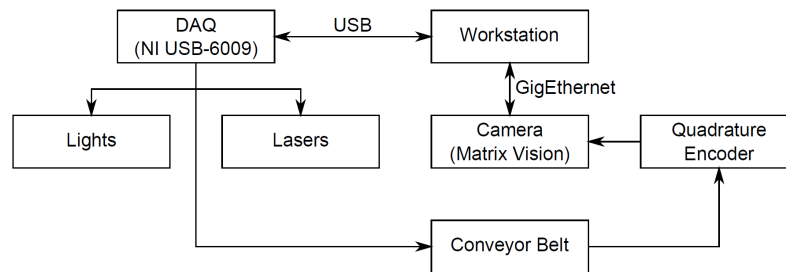


Fig. 12 Schematic of hardware components.

The total cost of building the 2.5D color scanner is $\sim \text{€}3000$. The conveyor belt, encoder, and digital I/O device are excluded, as they are assumed to be a part of the assembly line into which the system is integrated. Because the prices considered are the unit-piece purchase costs, the final cost can be expected to be reduced. Our system is 2-3 times less expensive than existing commercial sensors offering similar capability and performance.

3.5 Reconstruction density and resolution

The primary output of the 2.5D color scanner is a reconstruction of the scanned object in the form of a color point cloud, as shown in Fig. 13b. The density and resolution of this reconstruction is determined by a number of system parameters,

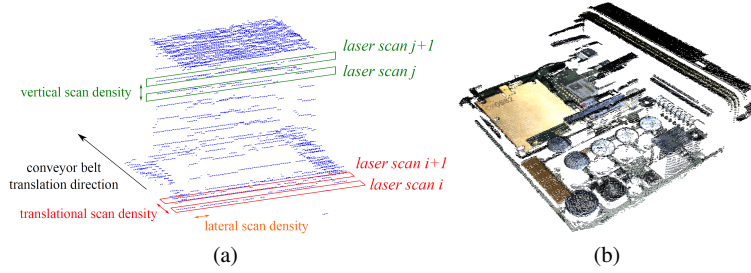


Fig. 13 (a) Reconstruction density of color point cloud. (b) Color point cloud reconstructed using our 2.5D color scanner.

including the camera frame rate (fps), the speed of the conveyor belt (v), the triangulation angle (α), and the camera to scene distance (Z), all of which can be adjusted to adapt to different inspection requirements. Fig. 13a illustrates the terms we use to characterize our reconstructed 3D models, while Table 1 gives the formulas for these characterizations, as well as the values for our current setup, with $fps = 28$, $v = 15mm/s$, $\alpha = 65^\circ$, $Z = 350mm$, $f = 16mm$, and $s_{z_{px}} = 4.4\mu m$. This reconstruction density and resolution are adequate for most of the completeness inspection tasks that we have considered, ranging from a small PCB board measuring $9 \times 12cm$ and $3cm$ high, to larger automotive components and heating elements measuring $20 \times 30cm$ and $10cm$ high.

Table 1 Reconstruction density and resolution.

<i>Parameter</i>	<i>Formula</i>	<i>Value</i>
Translation Scan Density	$\frac{v}{fps}$	$0.534mm$
Vertical Scan Density	$\frac{v}{fps} \tan \alpha$	$1.145mm$
Lateral Scan Density	$Z \frac{s_{z_{px}}}{f}$	$0.096mm$
Vertical Resolution	$Z \frac{s_{z_{px}} \tan \alpha}{f - s_{z_{px}} \tan \alpha}$	$0.207mm$

4 Sensor calibration

The calibration of the system involves the recovery of three sets of parameters (Fig. 14):

- camera intrinsic parameters (focal length f , principal point $[u_c, v_c]^T$, distortion coefficients)
- laser light plane parameters ($\hat{\mathbf{n}}_A, d_A, \hat{\mathbf{n}}_B, d_B$)
- translational direction of the conveyor belt ($\hat{\mathbf{t}}$).

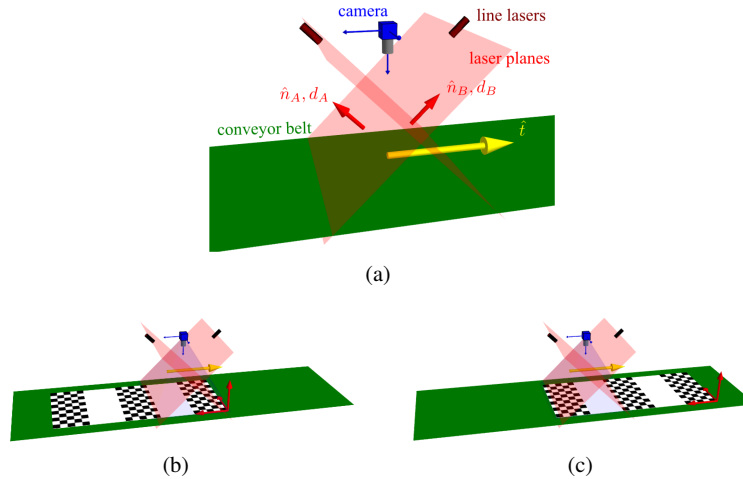


Fig. 14 (a) Sensor calibration parameters. (b) - (c) Calibration procedure using a planar checkerboard.

We refer to the recovery of these sets of parameters respectively as camera calibration, laser calibration, and conveyor calibration. McIvor [5] has given a holistic calibration procedure for a similar system that recovers all three sets of parameters simultaneously, but requires the use of a 3D calibration object. For our system, we have devised a simple procedure requiring only a planar checkerboard pattern (Fig. 14b-c). In addition to being easily and inexpensively produced, the checkerboard pattern can be readily detected using open-source software such as OpenCV, reducing the software development costs.

4.1 Misalignment between point clouds

The calibration method we devised is similar to mainly existing techniques for camera-laser calibration ([3], [2], [7], [14], [13]). However, for our dual-laser configuration, small errors in the calibration can result in a misalignment between the point clouds reconstructed with the two lasers, arising from an inconsistency between the laser plane parameters ($\hat{n}_A, d_A, \hat{n}_B, d_B$) and the conveyor motion (\hat{t}) when they are determined independently. As shown in Fig. 15, a reconstruction of the conveyor belt plane and a rectangular block reveals a significant offset between the point clouds of the two lasers. The offset in the vertical direction ranges from 3 – 5mm.

Fig. 16 illustrates for the 2D case how this misalignment depends on errors in calibration data. When laser calibration and motion calibration are performed separately, the misalignment cannot be detected from the calibration results.

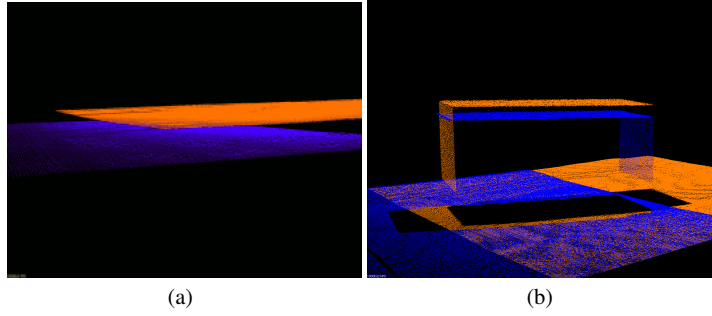


Fig. 15 Reconstructions showing offset between the point clouds of the two lasers. (a) Conveyor plane. (b) Rectangular block.

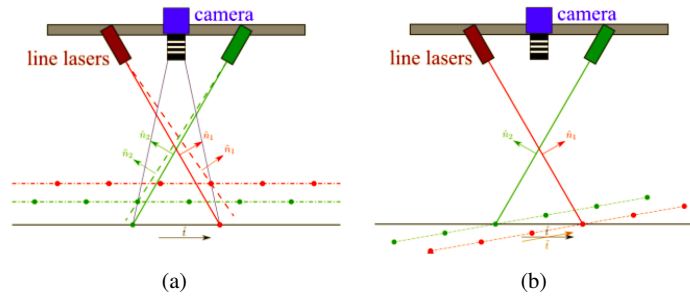


Fig. 16 Misalignment between the two laser point clouds in the reconstruction of a single plane due to (a) errors in laser parameters and (b) errors in translation direction.

4.2 Constrained calibration

In order to detect and correct the misalignment between the point clouds during calibration, a calibration procedure in which the calibration data is constrained by both the laser and motion parameters is required. We present two solutions; the first method uses the laser plane parameters to constrain the motion calibration, while the second method uses the motion parameters to constrain the laser calibration.

4.2.1 Constraining motion calibration with laser parameters

First, laser calibration is performed independently from motion calibration by using the method described in [9]. Next, motion calibration is performed as follows. A calibration board with three checkerboard patterns is placed parallel to the conveyor belt as illustrated in Fig. 14b-c. The line lasers are also turned on. Images of the checkerboard patterns and the laser lines are captured together at various positions, along with either the encoder counts ΔE_i or the timestamp Δt_i .

Using the laser plane parameters alone, the detected laser points are triangulated, giving their 3D coordinates with respect to the camera center. Because two line lasers are present, the laser range data can be used to determine the plane π_c of the calibration board. The plane parameters $\pi_c = (\hat{\mathbf{n}}_c, d_c)$ are recovered by finding the best-fit plane to all of the triangulated laser points. To recover the translational direction $\hat{\mathbf{t}}$ of the conveyor belt, we form a constrained pose estimation problem with the following constraints:

- because the calibration board is undergoing pure translation, all of the poses have the same rotation, $\mathbf{R} = \mathbf{R}_1 = \dots = \mathbf{R}_i$
- the translation $\vec{\mathbf{t}}_i$ from the camera to each checkerboard pose is offset from the first checkerboard pose $\vec{\mathbf{t}}_1$ in the same direction $\hat{\mathbf{t}}$, $\vec{\mathbf{t}}_i = \vec{\mathbf{t}}_1 + \mu_i \hat{\mathbf{t}}$
- all of the checkerboard poses $(\mathbf{R}_i, \vec{\mathbf{t}}_i)$ must lie on the calibration plane π_c defined by the laser points

where μ_i is the magnitude of the translation motion, $\hat{\mathbf{t}}$ is the translational direction being seek in the current motion calibration.

The third constraint is the additional contribution of using lasers in motion calibration. To perform this constrained calibration, we establish an arbitrary calibration pose $(\mathbf{R}_c, \vec{\mathbf{t}}_c)$ on the plane π_c , and minimize the following cost function:

$$\arg \min_{\psi, \vec{\mathbf{t}}_{c1}, \theta, v} \sum_j \left\| \mathbf{x}_j - \mathbf{K} \cdot [\mathbf{R} | \vec{\mathbf{t}}_i] \cdot \mathbf{X}_j \right\|^2 \quad (9)$$

Here, \mathbf{X}_j and \mathbf{x}_j are the checkerboard corners and their imaged coordinates, \mathbf{K} is the camera intrinsic parameters matrix, v is the speed of the linear motion platform, ψ is the angle of rotation of the checkerboard patterns from the calibration pose $\mathbf{R} = \mathbf{R}_c \cdot \mathbf{R}_z(\psi)$, and $\vec{\mathbf{t}}_{c1}$ is a 2D vector lying in the calibration plane π_c corresponding to the offset of the first checkerboard pose from the calibration pose, $\vec{\mathbf{t}}_1 = \vec{\mathbf{t}}_c + \mathbf{R}_c \cdot [\vec{\mathbf{t}}_{c1}^T, 0]^T$. Moreover, when the calibration board is placed parallel on the conveyor belt, $\hat{\mathbf{t}}$ must lie in the plane of the calibration board. This is parameterized using 1 DOF, $\hat{\mathbf{t}} = \cos \theta \hat{\mathbf{i}} + \sin \theta \hat{\mathbf{j}}$, where $\hat{\mathbf{i}} = \mathbf{R} \cdot [1 \ 0 \ 0]^T$ and $\hat{\mathbf{j}} = \mathbf{R} \cdot [0 \ 1 \ 0]^T$. Thus, the constrained problem has 4 to 5 DOF, corresponding to 3 DOF for the first checkerboard pose, 1 DOF for $\hat{\mathbf{t}}$, and 1 DOF for v if desired.

4.2.2 Constraining laser calibration with motion parameters

First, motion calibration is performed independently from laser calibration by using the method described in [9]. However, the laser lines are imaged together with the checkerboard patterns, and the process is repeated multiple times with the calibration board at different orientations \mathbf{R}^k (Fig. 17).

Using the correspondences $\{\mathbf{X}_j^k \leftrightarrow \mathbf{x}_j^k\}$ between the checkerboard corners and their imaged coordinates, a single translational direction $\hat{\mathbf{t}}$ is estimated for the entire data set by minimizing the following cost function:

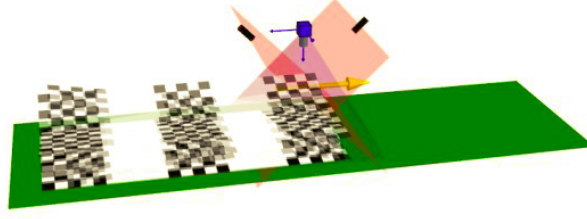


Fig. 17 Constrained laser calibration.

$$\arg \min_{\mathbf{R}^k, \vec{\mathbf{t}}_1^k, \theta, v} \sum_j \left\| \mathbf{x}_j^k - \mathbf{K} \cdot \left[\mathbf{R}^k \mid \vec{\mathbf{t}}_i^k \right] \cdot \mathbf{X}_j^k \right\|^2 \quad (10)$$

Here, $(\mathbf{R}^k, \vec{\mathbf{t}}_1^k)$ is the initial pose of the calibration board for orientation \mathbf{R}^k . We assume that one of the orientations \mathbf{R}^p is parallel to conveyor belt, so that the translational direction $\hat{\mathbf{t}}$ can still be parameterized using 1 DOF, $\hat{\mathbf{t}} = \cos \theta \hat{\mathbf{i}} + \sin \theta \hat{\mathbf{j}}$, where $\hat{\mathbf{i}} = \mathbf{R}^p \cdot [1 \ 0 \ 0]^T$ and $\hat{\mathbf{j}} = \mathbf{R}^p \cdot [0 \ 1 \ 0]^T$. For n_k different checkerboard orientations, the constrained problem has $6n_k + 1$ or $6n_k + 2$ DOF.

Using the checkerboard poses $(\mathbf{R}^k, \vec{\mathbf{t}}_i^k)$ and the laser points in the same images, laser calibration can be performed using the standard method described in [9].

4.2.3 Validation of constrained calibration

To validate the constrained calibration methods presented above, a plane is placed at ten different positions and scanned, and the offset between the point clouds reconstructed from the two lasers is measured. As shown in Fig. 18, when laser calibration and motion calibration are performed independently, the misalignment error ranges between 0.5 to 5mm. When the motion calibration or the laser calibration is constrained by the other set of parameters, the error is dramatically reduced to 1.0 and 0.4mm respectively.

5 3D Reconstruction

5.1 Reconstruction process and output products

Fig. 19 shows the pipeline of the reconstruction software developed for our Dual-Laser Triangulation System with a color camera, along with the different data products it produces. The laser points are detected in the images, triangulated and merged together by means of calibration to obtain a 3D point cloud of the scanned object,

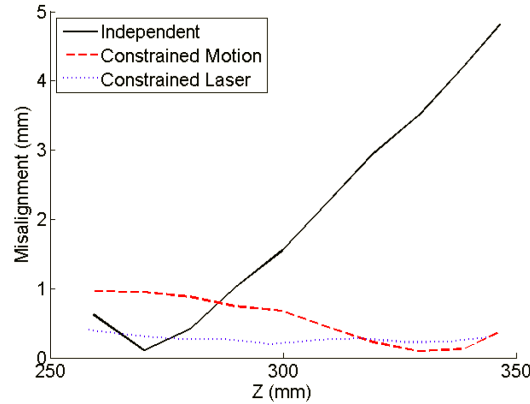


Fig. 18 Misalignment errors between the point clouds of the two lasers of a plane scanned at 10 different positions.

which can be used to derive a range image. On the other hand, the central part of each image contains texture which is used for creating a stitched image of the object or for texturing the 3D point cloud in order to obtain a direct correspondence between 3D and color information. The registered image is obtained superimposing the range image onto the texture image. Finally, a textured mesh can also be created from the colored point cloud for better visualization.

The different data representations can be exploited for different types of inspection tasks. For a detailed description on how these products are obtained, please refer to [8].

5.2 Software performance

Table 2 shows the average processing time per frame required for the 3D reconstruction steps, executed on a standard workstation (Intel Xeon E3-1225 quad-core @ 3.1GHz, 4GB memory). At a frame rate of 28.1 *fps*, the inter-frame interval is 35.6 *ms*. Thus, the reconstruction pipeline can perform in real-time.

The range image is generated after the entire point cloud has been constructed, and can be completed extremely quickly in the order of milliseconds. The registered texture image is generated as part of the point-cloud coloring and image-stitching processes. Therefore, performance time is not reported for these processes.

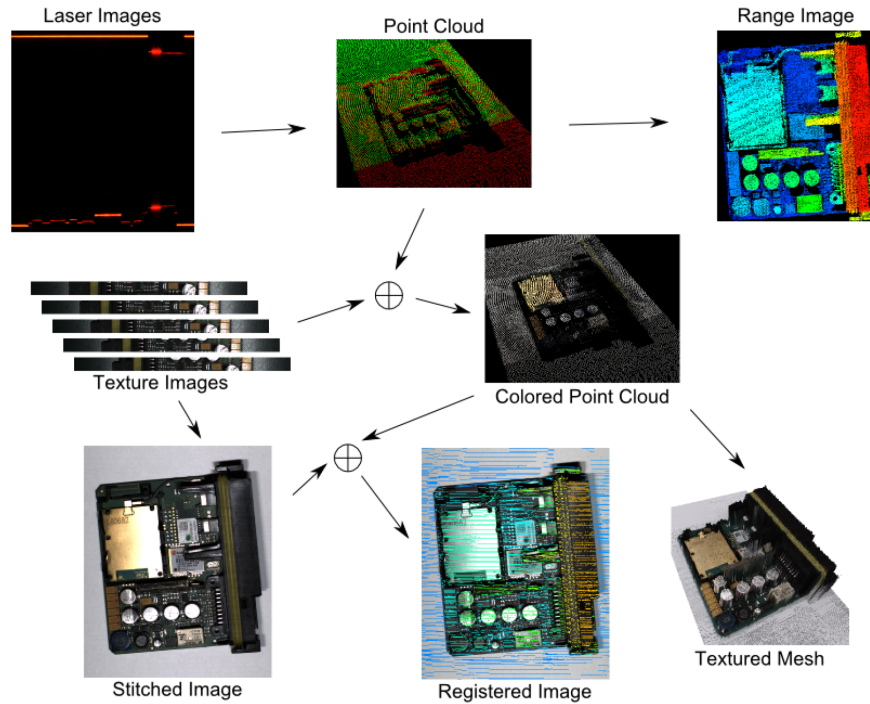


Fig. 19 Reconstruction pipeline and products.

Table 2 Processing time for reconstruction.

<i>Process</i>	<i>Time</i>
Laser detection and triangulation	16 ms
Point cloud coloring	1 ms
Texture stitching	5 ms
Total	22 ms

6 Completeness inspection

In this section, we report a number of examples of inspection tasks that can be solved by exploiting the products obtained in real time with the Dual-Laser Triangulation System described in the previous sections. While many of the algorithms are trivial, it exemplifies the ease with which a wide range of inspection tasks can be accomplished when aligned 3D and color information is available. The variety of data representations that is produced by our reconstruction software brings further flexibility in devising the inspection algorithms. In particular, we show how the color point cloud, the range image, the stitched texture image, and the registered texture image can be used effectively to solve different types of inspection tasks.

In some cases, quality inspection is obtained by aligning the scan of the object to inspect to a reference model which does not present defects and then by searching for components of interest at known positions or by comparing the models in a direct manner, as we will see in Section 6.5. For aligning new scans with a reference model, we exploit the pose estimation and model alignment method described in [8], which is based on Principal Component Analysis and alignment of plane clusters.

6.1 Inspection using color point cloud

As an example of complex inspection task which can be solved with the high resolution color point clouds, we report the cable inspection in Fig. 20. The task was to detect if a black cable with a 1mm diameter was correctly routed between two vertical black pegs 4mm high. This inspection task is very difficult to solve for traditional 2D visual inspection systems, because of the low contrast between the components. Instead, from our 3D point clouds we can easily isolate the pegs and the cable. Our approach aims at identifying clusters which are not only coherent in position and number of points, but also have a particular curved shape. For this purpose, we select only points with mean curvature above 0.01. The estimated cable points are highlighted in red, while the pegs are colored in green. It can be noticed that both the cable and the pegs are correctly detected in both the good and the faulty boards.

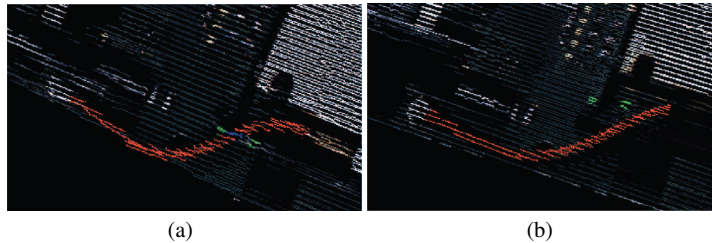


Fig. 20 Cable routing inspection using color point cloud. (a) Cable (red) correctly routed through pegs (green). (b) Incorrect cable routing.

6.2 Inspection using range image

Another common inspection task is to check if a component is present or absent. Fig. 21a shows a sample PCB where the fuses circled in red are to be checked. This is particularly difficult using the image alone, because the fuse is mostly a glass casing with a fine filament inside, and the ends of the fuse are metal caps that are the same color and shape as their clips. Using the point cloud also proved to be

difficult, because the sparse amount of points reflected off the glass do not allow them to be clustered together easily to be identified as a component. However, the range image in Fig. 21b gives a clear indication when they are present (component shows up as yellow, circled in white), and the range image in Fig. 21c gives a clear indication when they are absent.

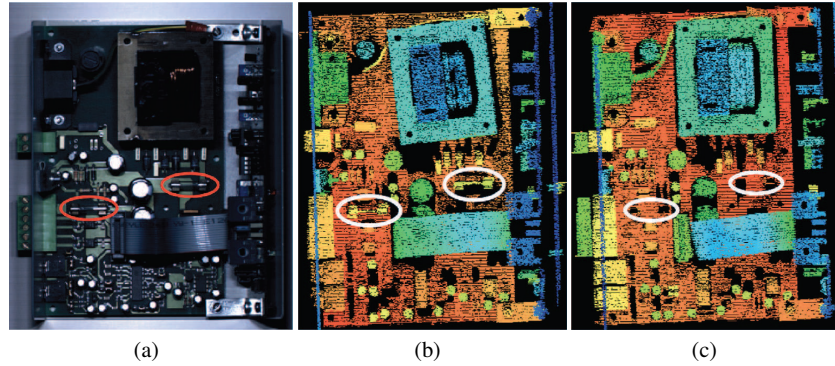


Fig. 21 Examples of inspection using range image. (a) Texture image showing location of clear fuses. (b) Range image showing presence of fuses. (c) Range image showing absence of fuses.

6.3 Inspection using stitched image

Another common inspection task is to check for the orientation of a component. In Fig. 22, the white two-pin connector on the right side of the image is to be checked, with Fig. 22a showing the correct orientation and Fig. 22d showing the incorrect orientation. Because the component is fairly small, the point cloud density is not high enough for the inspection to be made reliably using the point cloud (Fig. 22b and e) or the range image (Fig. 22c and f). However, the dense texture information allows this check to be accomplished using 2D image analysis by edge and contour detection, as shown in Fig. 22h.

6.4 Inspection using registered image

A rather unique inspection task requires that the number of loops in a coil to be counted, as shown in Fig. 23a.

The point cloud density is not high enough for each coil to be reconstructed consistently from end to end, as seen in the point cloud (Fig. 23b) and the range image (Fig. 23c). Inspection of the stitched texture image (Fig. 23d) shows that a possible

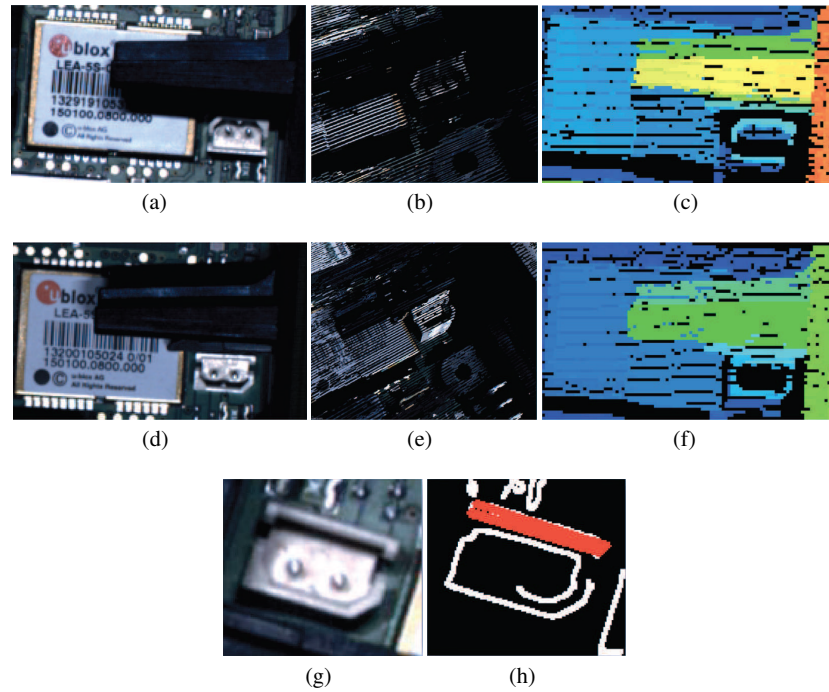


Fig. 22 Examples of inspection using texture image. (a) Correct texture image. (b) Correct point cloud. (c) Correct range image. (d) Incorrect texture image. (e) Incorrect point cloud. (f) Incorrect range image. (g) Detail of the texture image. (h) Edge and contour detection on texture image.

solution is to count the number of saturated pixels; however, saturated pixels can belong to the top or a bottom of a loop, and it is difficult to differentiate between the two using the texture image alone. The registered texture image (Fig. 23f) provides an elegant solution here, since the depth of the saturated pixels can be determined, allowing them to be classified reliably as either the top or bottom of a loop.

Given that only registered depth and texture data allow solving this problem, we showed a clear advantage of our system with respect to many more expensive commercial solutions which do not provide this kind of alignment.

6.5 Automatic change detection

Given that our system is highly repeatable in producing scans of an object and a new scan can be aligned to a reference point cloud, a direct method can also be applied to detect changes in a test point cloud with respect to a reference model. Fig. 24a is an example of a point cloud acquired from a correctly assembled board that serves as the reference. Fig. 24b shows the point cloud belonging to a board to be tested.

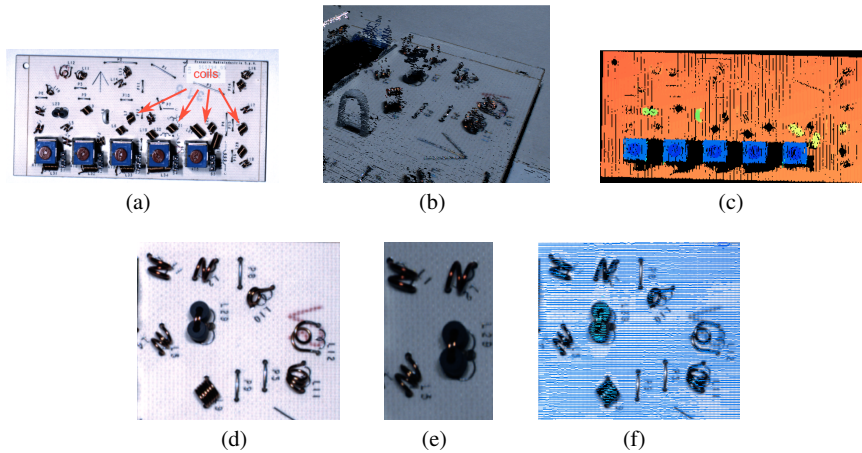


Fig. 23 Example of inspection using registered texture image. (a) Image showing location of coils to be inspected. (b) Color point cloud. (c) Range image. (d) Texture image. (e) Saturated pixels in texture image corresponding to coil elements. (f) Registered texture image used to determine depth of saturated pixels.

The input point cloud can be carefully aligned with respect to the reference point cloud, so that its points which do not have a correspondence in the reference model can be identified. A point is considered to have a correspondence in the reference cloud if its distance to the reference cloud is under a user-defined threshold. The use of a color point cloud also allows the distances to be computed in the XYZ-RGB or XYZ-HSV space, instead of the XYZ space. By using an octree data structure to represent the point cloud, a very fast computation of points neighbors is obtained. As it can be noticed in Fig. 24b, where the points without correspondence are colored in red, the black cable at the bottom of the figure is detected as misplaced. Some small differences between the two point clouds due to outliers or border effects are also detected, but these can be easily removed by filtering out small differences.

7 Industrial application

The hardware and software presented in this work also led to a new industrial solution called *Smart Check 3D*, produced and sold by IT+Robotics srl. It allows 3D completeness inspection of products on a production line. Smart Check 3D is available either as flexible scanning system mounted on a manipulator arm (Fig. 25a) or as inspection tunnel within a production line which allows to reach the maximum scanning speed.

In Fig. 25b, a picture of an object which had to be inspected by our system is reported, while the 3D point cloud obtained from a single scan is reported in Fig. 25c. Red color highlights the part of the scan which is considered as consistent

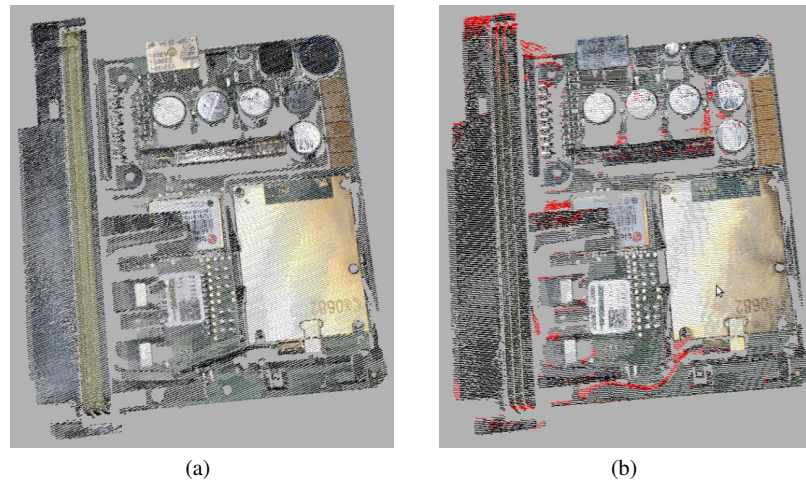


Fig. 24 Automatic change detection. (a) Reference point cloud. (b) Test point cloud with differences in red.

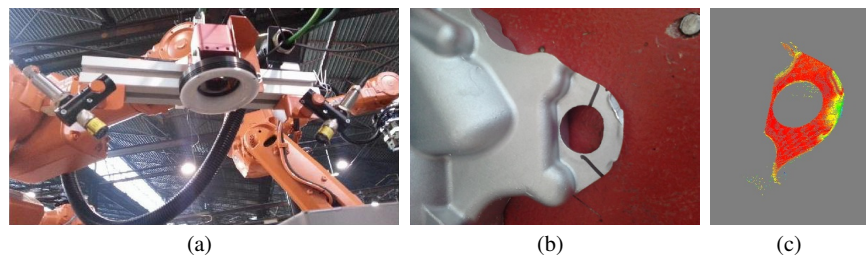


Fig. 25 (a) Industrial version of the Dual-Laser Triangulation System proposed in this work. (b) Part to be scanned. (c) 3D point cloud resulting from the scan with color-coded quality inspection.

with the CAD model of the object, while yellow and green colors show the parts where there are deviations from the model, thus those parts which are defective.

8 Conclusions

In this chapter, we presented the 2.5D color scanner we developed for real-time 3D color reconstruction of objects within a production line for the purpose of completeness inspection in 3D. We also detailed the calibration procedure that allowed us to reach very high accuracy in the reconstruction without the need for complex calibration objects. The wide range of output products that our software can provide proved to be very effective for performing inspection tasks which would be

extremely difficult to solve for state-of-the-art 2D-based methods. Finally, we show that our system has already been integrated into a real industrial solution.

As a future work, we envision to also test our system with cameras with onboard processing, which could further improve the scanning speed.

Acknowledgements This research has been funded by the European Unions 7th Framework program managed by REA Research Executive Agency (<http://ec.europa.eu/research/rea> - FP7/2007-2013) under grant agreement No. 262009, *3D Complete* project.

References

1. Z. Bi and L. Wang. Advances in 3d data acquisition and processing for industrial applications. *Robotics and Computer-Integrated Manufacturing*, 26:403–413, 2010.
2. C. Chen and A. Kak. Modeling and calibration of a structured light scanner for 3-d robot vision. In *International Conference on Robotics and Automation*, volume 4, pages 807–815, 1987.
3. D.Q. Huynh, R.A. Owens, and P.E. Hartmann. Calibrating a structured light stripe system: a novel approach. *International Journal of Computer Vision*, 33:73–86, 1999.
4. E.N. Malamas, E.G.M. Petrakis, M. Zervakis, L. Petit, and J.-D. Legat. A survey on industrial vision systems, applications and tools. *Image and Vision Computing*, 21:171–188, 2003.
5. A.M. McIvor. Non-linear calibration of a laser stripe profiler. *Optical Engineering*, 41:205, 2002.
6. N. Pears, Y. Liu, and P. (Eds.) Bunting. *3D Imaging, Analysis and Applications*. Springer, 2012.
7. I.D. Reid. Projective calibration of a laser-stripe range finder. *Image and Vision Computing*, 14:659–666, 1996.
8. Edmond So, Matteo Munaro, Stefano Michieletto, Emanuele Menegatti, and Stefano Tonello. 3dcomplete: Efficient completeness inspection using a 2.5d color scanner. *Computers in Industry - Special Issue on 3D Imaging in Industry, Elsevier*, 64(9):1237–1252, 2013.
9. E.W.Y. So, S. Michieletto, and E. Menegatti. Calibration of a dual-laser triangulation system for assembly line completeness inspection. In *IEEE International Symposium on Robotic and Sensors Environments*, pages 138–143, 2012.
10. W. Stocher and G. Biegelbauer. Automated simultaneous calibration of a multi-view laser stripe profiler. In *IEEE International Conference on Robotics and Automation*, pages 4424–4429, 2005.
11. E. Trucco, R. B. Fisher, A. W. Fitzgibbon, and D. K. Naidu. Calibration, data consistency and model acquisition with laser strippers. *International Journal of Computer Integrated Manufacturing*, 11:292–310, 1998.
12. J.a.L. Vilaça, J.C. Fonseca, and A.M. Pinho. Calibration procedure for 3d measurement systems using two cameras and a laser line. *Optics and Laser Technology*, 41:112–119, 2009.
13. K. Yamauchi, H. Saito, and Y. Sato. Calibration of a structured light system by observing planar object from unknown viewpoints. In *International Conference on Pattern Recognition*, pages 1–4, 2008.
14. F. Zhou and G. Zhang. Complete calibration of a structured light stripe vision sensor through planar target of unknown orientations. *Image and Vision Computing*, 23:59–67, 2005.